MNE 32 (2026) 100382

Contents lists available at ScienceDirect

Micro and Nano Engineering

journal homepage: www.sciencedirect.com/journal/micro-and-nano-engineering

Research paper

# Standing waves-induced surface roughness in grayscale lithography

Hedir Melissa [a,*], Picca Axel [a], Gerges Nadine [a,b], Rahali Ayoub [a], Denaix Lou [a], Carcenac Alexis [c], Gousset Silvère [c], Ferrec Yann [b], Gourgon Cécile [a]

[a] Univ. Grenoble Alpes, CNRS, CEA/LETI-Minatec, Grenoble INP, LTM, 38054 Grenoble, France
[b] ONERA/DOTA, BP 80100, Chemin de la Hunière, 91123 Palaiseau, France
[c] Institut de Planétologie et d'Astrophysique de Grenoble, Université Grenoble-Alpes, 38058 Grenoble, France

ARTICLE INFO

*Keywords:*
Grayscale lithography
Standing waves
Surface roughness
Interferometric devices

ABSTRACT

Grayscale lithography is a powerful technique for the fabrication of three-dimensional microstructures, particularly for optical applications requiring precise thickness control. However, optical interference effects within the photoresist, such as standing waves, can significantly affect both the developed resist profile and the resulting surface quality. In this work, we experimentally investigate the influence of standing waves on surface roughness in grayscale lithography and its subsequent transfer into silicon using one-dimensional staircase structures fabricated by Digital Micromirror Device (DMD)–based grayscale exposure. We show that standing-wave-induced dose modulations not only produce oscillations in the developed resist thickness but also lead to pronounced surface roughness maxima at specific exposure doses. These roughness features are amplified during inductively coupled plasma etching (ICP) into silicon, directly impacting the final topography. We further investigate two mitigation strategies—post-exposure bake (PEB) and bottom anti-reflective coatings (BARC). This study highlights the impact of standing waves on the generation of surface roughness in grayscale lithography and suggests approaches for controlling these effects in silicon micro-optical structures.

## 1. Introduction

Grayscale lithography has become an essential technique for fabricating complex 3D microstructures [1–3], particularly in micro-optics [4,5], MEMS [6–9], and diffractive devices [10]. Unlike binary lithography, where features are defined by a simple exposure/no-exposure process, grayscale lithography relies on locally modulating the exposure dose to create continuous relief profiles. This method allows precise realization of optical elements such as microlenses [11–13], blazed gratings [14], metasurfaces [4,15], and interferometric components [16]. One of the key challenges in grayscale lithography lies in accurately mapping the exposure dose to the resist profile, which depends on resist contrast, process conditions, and optical effects such as standing waves. In photoresists, standing waves are formed when incident light penetrates the resist and interferes with light reflected from the resist–substrate interface, creating a periodic intensity distribution along the resist thickness [17,18]. Another challenge in grayscale lithography is controlling surface quality. Surface roughness strongly affects device performance, especially in optical applications, where scattering losses or phase distortions can significantly reduce efficiency [19–21]. Several factors contribute to surface roughness, including intrinsic resist properties such as polymer chain morphology [22], developer diffusion effects during dissolution, and etch transfer processes [9,23,24]. In addition, optical phenomena such as interference and reflections at the resist–substrate interface can also modify the final resist profile. In this paper, we experimentally investigate the effect of standing waves on surface roughness. We demonstrate that local overexposure at specific depths within the photoresist leads to an increase in surface roughness. This work is carried out in the framework of the European SCARBOn project, which aims at developing compact SWIR imaging spectrometers for greenhouse gas monitoring. These instruments rely on arrays of silicon Fabry–Perot (FP) cavities with controlled step heights to sample specific optical path differences associated with SWIR absorption features. Their fabrication requires producing stepped silicon patterns with nanometric vertical resolution over a large area ($\sim 1 cm^2$), making surface quality a critical parameter. In this paper, we focus on the lithographic and etching aspects governing this surface quality, while the detailed device context is provided in the Supplementary Material.

Within our research group, grayscale lithography and silicon etching

* Corresponding author.
*E-mail addresses:* melissahedir@gmail.com (H. Melissa), cecile.gourgon@cea.fr (G. Cécile).

https://doi.org/10.1016/j.mne.2026.100382
Received 21 January 2026; Received in revised form 16 July 2026; Accepted 1 August 2026
Available online 4 August 2026
2590-0072/© 2026 The Authors. Published by Elsevier B.V. This is an open access article under the CC BY license (http://creativecommons.org/licenses/by/4.0/).

processes have been developed for the fabrication of silicon interferometric plates featuring staircase geometries with nanometric step heights. Fig. 1.a shows a wafer patterned with 2D arrays of 960 × 960 $\mu m^2$ Fabry–Perot (FP) interferometers before silicon etching. Colors indicate different resist thicknesses in the staircase geometry. Fig. 1.b presents an example of an etched silicon interferometric plate, where some steps appear slightly dull due to locally increased surface roughness. As mentioned above, the present study focuses on characterizing this roughness in the resist, evaluating its transfer into silicon, and understanding why it occurs on certain steps but not others. To the best of our knowledge, no previous studies have explicitly linked surface roughness to standing waves in grayscale lithography. While several works have investigated surface quality in lithography in general and in grayscale lithography in particular, most have focused on line edge roughness [25,26] rather than the topography of planar surfaces. A few studies have addressed surface roughness in positive photoresists for micro-optical structures fabrication [19,21,27], and suggested approaches such as post-exposure bake (PEB) or thermal reflow to smooth the resist surface. However, none have systematically explored the role of standing waves in generating or enhancing this roughness. This gap motivates the present work, in which we experimentally examine how standing wave effects influence surface roughness in photoresist patterns and their subsequent transfer into silicon. In addition, we investigate potential solutions to attenuate standing-wave–induced roughness, such as post-exposure bake (PEB) and the use of bottom antireflective coatings (BARC). The latter has been widely studied in lithography as an effective strategy to control reflectivity and improve lithography performance [28].

## 2. Experimental process

We fabricated our interferometric plates using SmartPrint UV system supplied by Microlight3D, a maskless grayscale lithography tool that projects UV light (385 nm) through a Digital Micromirror Device (DMD). The DMD modulates the exposure dose pixel by pixel using time-modulated grayscale, enabling precise control of local intensity without physical masks [29]. A positive Novolak/DNQ photoresist (ma-P1225G, MicroResist Technology GmbH) was diluted 1:1 with solvent and spin-coated at 3000 rpm for 30 s to achieve a film thickness of ~ 480 nm on 100 mm silicon wafers. A soft bake at 130 °C for 35 s was applied. These conditions were optimized within our research group and, as demonstrated in Reference [16], increasing the soft-bake temperature leads to a reduction in resist contrast, which is essential for achieving the high vertical resolution required for the final device. The samples were exposed according to the grayscale design, then developed in mr-D526/S for 30 s. The grayscale design is implemented as a bitmap image with 255 Gy levels, corresponding to the pixel resolution of the SmartPrint UV system. Each pixel represents a specific exposure dose, with 255 corresponding to maximum exposure (white) and 0 to no exposure (black). Intermediate gray levels deliver proportionally lower doses, enabling continuous modulation of the resist profile. The UV exposure induces chemical transformations that render the exposed regions soluble in the aqueous TMAH-based mr-D526/S developer. Concretely, the diazonaphthoquinone (DNQ) groups in the resist absorb UV photons and undergo a Wolff rearrangement, converting them into carboxylic acid groups. These newly formed carboxylic acids are soluble in the basic developer, enabling selective dissolution of the exposed regions. Subsequent etching transfers the relief pattern into silicon, producing stepped interferometric plates in a staircase geometry (see the scheme of Fig. 2). The etching process is detailed in Reference [16]. The plates required by the SCARBOn project are organized in a 2D array, but the present work is focused on 1D shape as illustrated in the optical microscope images in Fig. 2. This choice of a 1D structure allows us to simplify the study and focus on the effects of standing waves, as a full 2D array would require significantly longer characterization times and more complex analysis.

Within the SCARBOn project, the target step height is 30 nm. Given that the etching process exhibits a selectivity of about 3, the corresponding resist profile must therefore be defined with a vertical resolution on the order of 10 nm. To assess whether this level of precision can be achieved, we analyzed the contrast curve to gain insight into the resist's development behavior. We first conducted a preliminary study to investigate the influence of stripe width on the contrast curve and the resulting resist profile and to determine the optimal dimensions of the exposed pattern. For this purpose, a series of test patterns consisting of parallel stripes with varying widths—from 10 µm to 960 µm—were fabricated using the same grayscale virtual mask containing 10 Gy levels ranging from 25 to 250, with increments of 25. This study aimed to evaluate how stripe width influences the uniformity of exposure and the resulting resist profile. The height of each step was measured using a profilometer, and the resulting contrast curves (developed thickness versus UV exposure dose) are shown in Fig. 3.a. Measurements were performed on the same wafer under different exposure conditions. In the first case, a 2.5× microscope objective was used with an exposure time of 2 s (orange curves), while in the second case, a 1× objective was used with an exposure time of 8 s (blue curves). The 2.5× objective was employed for the smaller-width stripes to achieve finer resolution, whereas the 1× objective was used for the larger-width stripes in order to avoid field stitching during exposure. As can be observed in Fig. 3.a, the resulting contrast curves are not smooth but exhibit distinct oscillations. When UV light penetrates the photoresist, part of it is reflected at the substrate interface, which in our case is silicon. The interference between the incident and reflected waves creates a periodic intensity distribution along the resist thickness, with alternating maxima (antinodes) and minima (nodes), known as standing waves. This produces a vertical modulation of the absorbed UV dose, even when the surface exposure is uniform. In the absence of such effects, the resist contrast curve would be monotonic. However, standing waves induce oscillations in this curve, known as “swing curve” [30], by locally affecting the photochemical conversion of DNQ to carboxylic acid. Regions

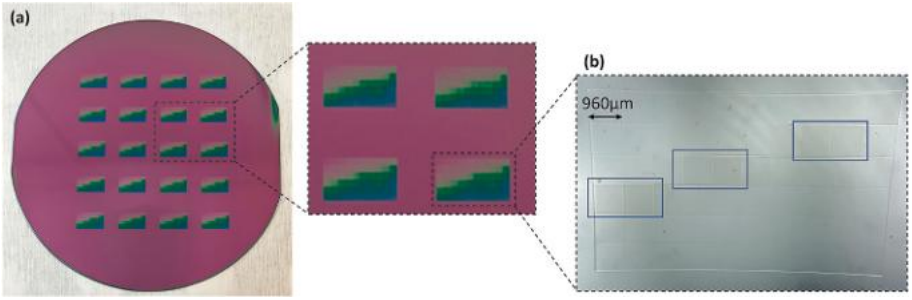


**Fig. 1.** (a) Macroscopic overview of the 100 mm lithographed wafer on ma-P 1225G resist. Each patterned area corresponds to an array (10 × 6) of 960 × 960 $\mu m^2$ steps exposed using a virtual grayscale mask. The different colors within each pattern indicate variations in the developed resist thickness. (b) Magnified view of one etched silicon interferometric pattern.

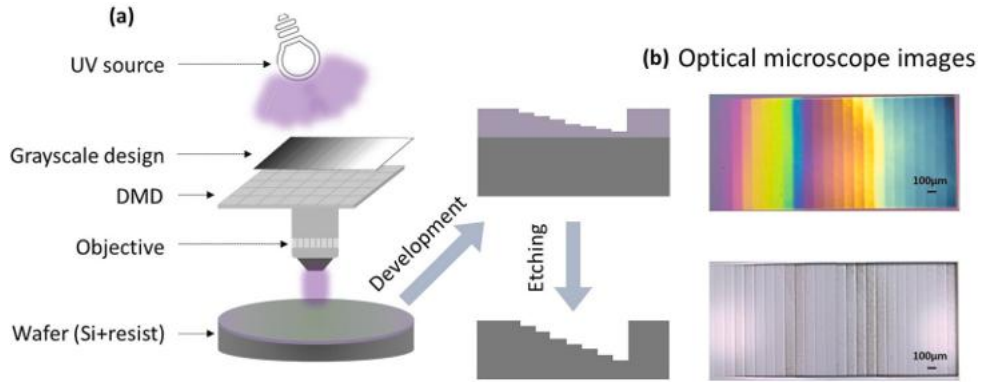


**Fig. 2.** (a) Schematic of the grayscale DMD projection system used for spatially modulated exposure. (b) Optical microscope images of the resulting one-dimensional staircase structures: resist profile (multicolor image) and corresponding etched silicon profile (gray image).

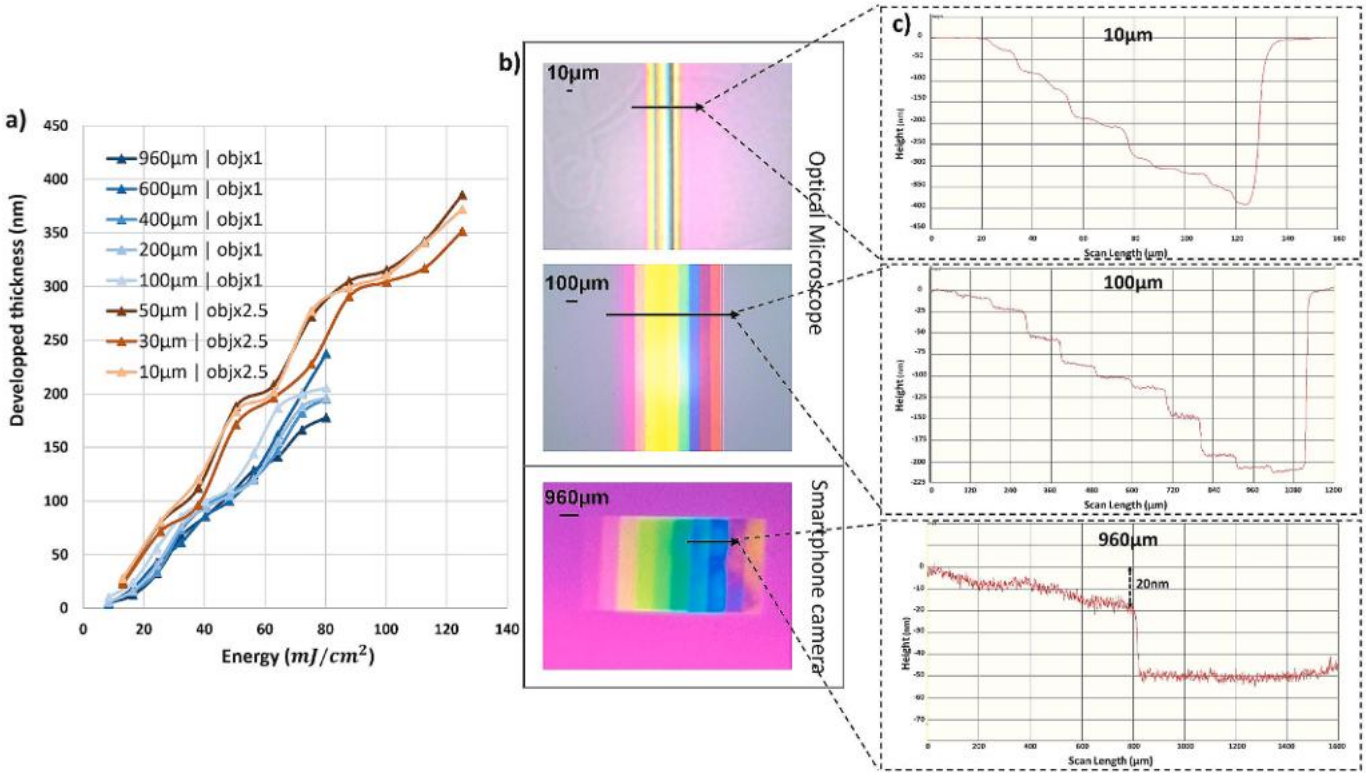


**Fig. 3.** (a) Contrast curves showing developed resist thickness as a function of exposure energy for stripe widths ranging from 10 µm to 960 µm. (b) Optical microscope images of developed resist patterns for three representative widths: 10 µm, 100 µm, and 960 $\mu$m. (c) Staircase profile obtained for: 10 $\mu$m, 100 $\mu$m, and 960 $\mu$m stripes width, measured with a mechanical profilometer.

corresponding to intensity maxima receive a higher effective dose, dissolve more rapidly during development, and result in non-uniform resist profiles with irregular step heights. The oscillation period of the swing curve corresponds approximately to $\lambda/(2n)$, where $\lambda$ is the exposure wavelength and $n$ the refractive index of the resist [31]. These oscillations appear consistently for all stripe widths, indicating that the standing-wave pattern is reproducible and independent of the stripe size.

The illumination intensities associated with the 1× and 2.5× objectives were characterized experimentally. Since the magnification $M$ of an objective determines the illumination intensity through an $M^2$ dependence, the expected ratio between the two configurations is simply given by the square of their magnifications. In this case, the 1× objective corresponds to $M = 1$ and the 2.5× objective to $M = 2.5$, leading to an intensity ratio of 1/6.25. Based on these measurements, the exposure times were chosen such that the resulting energies remained of the same order of magnitude for both objectives ($t_{exp} = 2$ s for 2.5× and $t_{exp} = 8$ s for 1×), enabling a consistent comparison of the resist response. The detailed procedure used to determine the intensity ratio and the corresponding exposure energies is provided in the Supplementary Material. With an exposure time of 2 s for the 2.5× objective and 8 s for the 1× objective, the corresponding energy ratio is approximately 1.56, indicating that the patterns illuminated with the 2.5× objective receive a larger dose. This increased dose naturally results in a deeper resist development, which is consistent with the orange curves of Fig. 3.a reaching thicknesses of about 400 nm, compared with about 200 nm for the 1× configuration. The larger developed thickness reflects the higher degree of DNQ conversion induced by the greater exposure energy. We observed the fabricated staircase structures using an optical microscope and illustrated some representative examples in Fig. 3.b. For

the larger-width stripes, the entire pattern could not be captured within a single microscope field of view; therefore, a smartphone camera was used to obtain global images of the full staircase. For the smallest-width stripes (10 μm), the contours between adjacent steps appear blurred in the optical microscope image. This effect is mainly attributed to the limited optical resolution relative to the step dimensions and to the finite slope transition between adjacent levels, which causes partial light scattering and reduces image contrast. In this case, the lateral extent of the slope is comparable to the stripe width, making it difficult to clearly distinguish the boundaries between consecutive steps. This observation is consistent with the profilometer measurement shown in Fig. 3.c, where the staircase profile reveals a continuous slope between steps rather than sharp transitions. Consequently, the stripes must be sufficiently wide compared to the slope transition region to ensure a well-defined staircase profile. In the case of the largest stripes (960 μm), another issue arises concerning the uniformity of exposure. In particular, the deepest steps exhibit visible non-uniform coloration, indicating a non-flat or uneven surface relief (see Fig. 3.b). This observation is confirmed by the mechanical profilometer measurements of Fig. 3.c, where the left-hand step shows a clear height modulation of approximately 20 nm across the width of one strip. Such a deviation is critical when targeting step heights on the order of 30 nm. This effect is attributed to the limited illumination homogeneity of the SmartPrint UV projection system over large exposure fields, which leads to spatial variations in the delivered dose and, consequently, in the developed resist profile. The origin and quantification of this inhomogeneity are discussed in detail in the Supplementary Material. From this analysis, we found that the best trade-off between well-defined steps and homogeneous exposure is achieved for a stripe width of 100 μm. As shown in Fig. 3.b, this configuration yields clearly defined and uniformly colored

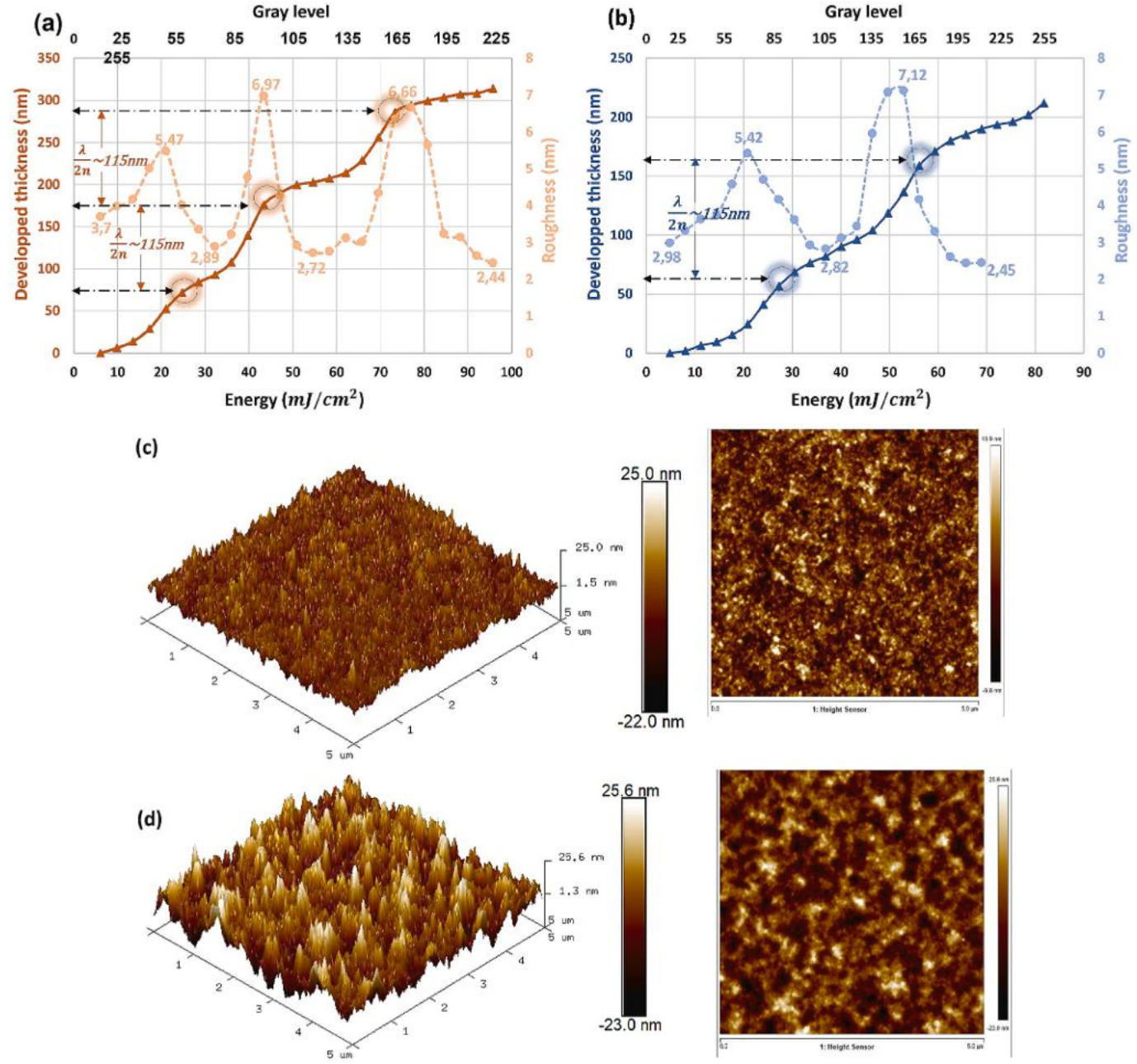


**Fig. 4.** (a,b) Developed thickness (contrast curve, left axis) and corresponding AFM surface roughness $R_q$ (right axis) plotted as a function of exposure energy for two exposure conditions: 2.5× objective with $t_{exp}$ = 1.5 s (a) and 1× objective with $t_{exp}$ = 8 s (b). (c,d) AFM topography images of two representative stripes exhibiting low (c) and high (d) surface roughness.

steps. The corresponding profilometer measurement in Fig. 3.c shows that the steps are sufficiently wide for the slope transition between adjacent levels to be negligible, resulting in a sharp and regular staircase profile. These results allowed us to select suitable stripe dimensions that ensure homogeneous exposure and well-defined step geometry for the subsequent fabrication of one-dimensional staircase structures, while confirming that the standing-wave-induced oscillations observed in the contrast curves are reproducible and independent of stripe width.

## 3. Standing waves and surface roughness

In the following, we employed another grayscale virtual mask containing 25 Gy levels ranging from 15 to 255, with increments of 10, to fabricate a one-dimensional staircase structure, increasing the number of measurement points for a more detailed characterization of the resist response. We fabricated our staircase structures on the same wafer using two different exposure conditions: a 2.5× objective with an exposure time of $t_{exp} = 1.5$ s and a 1× objective with an exposure time of $t_{exp} = 8$ s. The resulting contrast curves, shown in Figs. 4.a and 4.b, exhibit clear oscillations, reflecting the vertical modulation of the UV dose caused by interference effects within the resist. As previously observed, the 2.5× objective induces a deeper developed resist profile, reaching approximately 300 nm (see Fig. 4.a), whereas the 1× objective results in a total developed thickness of around 200 nm (see Fig. 4.b). These two conditions were deliberately chosen to create different total resist depths in order to investigate the behavior of standing waves at varying depths. In the orange curve, we observe three maxima corresponding to standing-wave oscillations, whereas in the blue curve only two maxima are visible. This difference arises because the higher energy delivered with the 2.5× objective allows the resist to develop more deeply, thereby sampling a larger portion of the standing-wave pattern. For thicker resists ($> 1\ \mu m$), the standing-wave period remains unchanged because it depends only on the exposure wavelength and on the refractive index of the resist, so a larger number of oscillation peaks would be present across the resist thickness. Such an accumulation of oscillation cycles evokes the line-edge-roughness (LER) effect observed in binary lithography. While the exact roughness amplitude may differ and would require dedicated measurements, the same interference mechanism is expected to occur. The spacing between the oscillation maxima agrees well with the theoretical standing-wave period, which is approximately 115 nm for a resist with refractive index $n = 1.6$ under UV exposure at $\lambda = 385\ nm$, as shown in Fig. 4. The surface roughness of each step was also measured using an Atomic Force Microscope (AFM), and the results are presented in the light-colored curves of Figs. 4.a and 4.b. Similar to the contrast curve, the roughness curve exhibits oscillatory behavior. Interestingly, the sample exposed with the higher energy shows three roughness maxima, while the lower-energy sample displays only two, matching the trend observed in the contrast curves. This correlation suggests a first hypothesis that the observed roughness peaks are directly related to standing-wave effects within the resist. Each roughness maximum systematically appears on the largest step of a given oscillation cycle, which corresponds to the steepest slope of the swing-curve peak in the contrast curve. In this dose region, the resist dissolves very rapidly during development, making the final surface profile highly sensitive to local variations in absorbed dose. For example, in Fig. 4.a, the first roughness maximum of $R_q = 5.47$ nm occurs at an exposure energy of approximately $E = 21\ mJ/cm^2$. This dose corresponds to the sharp rising slope of the first peak in the contrast curve. At this location, the dissolution rate increases abruptly with exposure, and the standing-wave modulation of the absorbed dose is not yet averaged out by the development process. As a result, the vertical dose non-uniformities induced by standing waves are directly transferred into the resist topography, producing an enhanced surface roughness. Figs. 4.c and 4.d show AFM scans acquired on regions of low and high surface roughness, respectively. The scan in Fig. 4.d, corresponding to an area located on a standing-wave-induced peak with a measured $R_q$ of 6.97 nm, displays a visibly textured surface with pronounced height variations. In contrast, Fig. 4.c, where the roughness is only 2.89 nm, exhibits a much smoother and more uniform topography, corresponding to a region situated between two peaks.

To transfer the patterns into silicon, we used an inductively coupled plasma (ICP) process on an Applied Materials tool with gas flows of 40 sccm $Cl_2$, 5 sccm $He/O_2$, and 120 sccm HBr. This process was chosen for its speed, reproducibility, and compatibility with different photoresists [16]. The reactor is equipped with in-situ optical monitoring, enabling accurate determination of the silicon etch rate. The total etch duration was ∼ 500 s, after which the residual photoresist was stripped in the same chamber using an oxygen plasma. Since the etch rate in silicon is higher than in the resist, the process exhibits a selectivity of approximately 3, defined as $S = \frac{R_{Si}}{R_{resist}}$, where $R_{Si}$ and $R_{resist}$ are the etch rates of silicon and resist, respectively. The selectivity is determined from the ratio between the thickness etched in silicon and the thickness developed in the resist, yielding an average value of about 3 for all the stripes. Fig. 5.a shows the total etched depth for each step, plotted as a function of the exposure energy, for the sample exposed with a 2.5× objective for 1.5 s. For comparison, the corresponding resist contrast curve is also shown using different vertical scales. The good superposition between the two curves demonstrates that the oscillatory behavior observed in the resist is accurately transferred to the silicon pattern. Three distinct maxima are clearly reproduced in the etched profile, consistent with the standing-wave-induced peaks measured in the resist. The total etched depth in silicon reaches approximately 1000 nm, confirming the selectivity of the process discussed above. In addition, we plotted the surface roughness of the etched silicon steps as a function of the exposure energy, obtained from AFM measurements (see Fig. 5.b). Similar to the contrast curve, the roughness curve exhibits three distinct maxima that align with the standing-wave-induced peaks, indicating that the roughness modulation generated in the resist is also transferred into the silicon. The baseline roughness and peak amplitudes are higher in silicon than in the resist. This amplification can be attributed to the higher etch rate of silicon compared to the resist. This is further confirmed by the optical microscope image shown in Fig. 5.c, where the etched depth corresponding to each grayscale level is superimposed onto the silicon staircase. Each step represents one gray level from the mask, allowing a direct visual correlation between the local etched depth and the physical appearance of the structure. Notably, the steps associated with etch-depth maxima exhibit visibly textured regions, indicating an increased surface roughness that mirrors the peaks observed in both the resist and the silicon depth measurements. This qualitative observation corroborates the quantitative analysis presented above. Overall, the figure demonstrates that standing-wave effects in the resist directly govern the final silicon topography. In the specific context of the SCARBOn project, these roughness values—even at the maxima—do not compromise the performance of the interferometric device. This is because only a small number of steps exhibit increased roughness, while the majority of the staircase remains well within acceptable optical quality. As a result, the global interferometric response remains unaffected; significant degradation would occur only if high roughness were present across all steps, which is not the case here. The optical function of the component is primarily determined by the uniformity and flatness of each step surface. The measured roughness levels stay well below the thresholds that would induce significant scattering or phase distortion. However, in a broader context of micro-optical fabrication, such roughness levels may become problematic. The combination of the intrinsic resist surface quality, the etch-rate contrast between resist and silicon, and the standing-wave–induced modulation can significantly amplify surface texture during plasma etching. For applications involving high-quality optical surfaces (such as waveguides, lenses, gratings, or resonant cavities) even moderate surface roughness can introduce additional optical losses, scattering, or reduced device accuracy. For these reasons, exploring strategies to reduce standing-wave-induced roughness is of

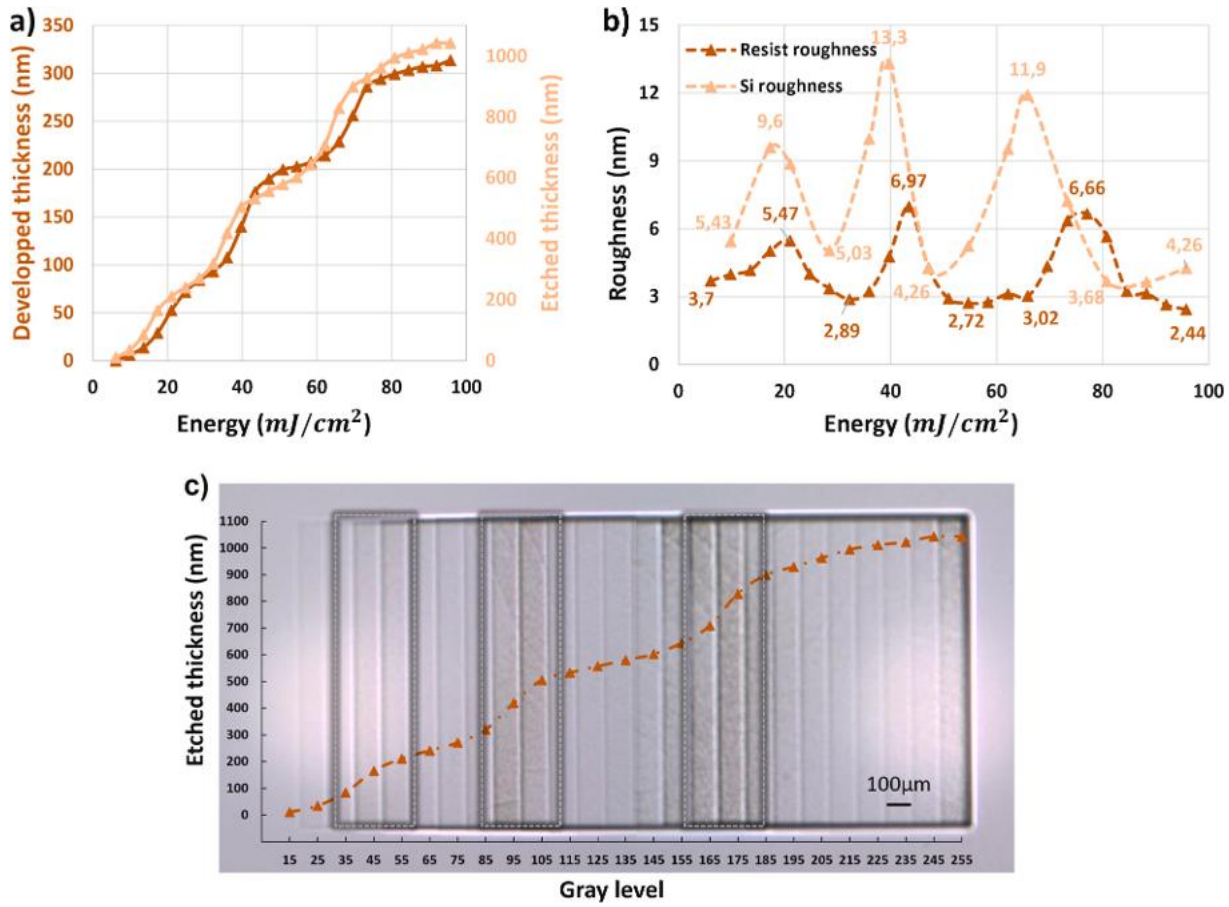


**Fig. 5.** (a) Comparison between the developed resist thickness (left vertical axis) and the etched silicon depth (right vertical axis) as a function of exposure energy. (b) AFM-measured surface roughness for the resist (dark orange curve) and for the etched silicon (light orange curve). (c) Optical microscope image of the one-dimensional staircase structure, with the measured silicon etched depth superimposed as a function of the applied grayscale level. (For interpretation of the references to colour in this figure legend, the reader is referred to the web version of this article.)

particular interest.

## 4. Strategies for surface roughness control

To mitigate the surface roughness maxima associated with standing-wave antinodes, we investigated two different approaches. The first one consists in the implementation of a post-exposure bake (PEB) treatment. The PEB enhances molecular diffusion and thermal relaxation within the polymer. Increasing the temperature enables the redistribution of the photogenerated carboxylic acid throughout the resist thickness, leading to a more homogeneous chemical profile before development. In our experiments, a PEB was performed at 90 °C for 5 min. Fig. 6.a shows the contrast curves of two samples: one subjected to PEB and one without. The sample with PEB (green curve) exhibits a slightly reduced slope in the contrast curve compared to the unbaked sample. The oscillations linked to standing waves are weakly reduced and remain well defined. Fig. 6.b presents the corresponding AFM surface roughness measurements for the same samples. The PEB leads to a modest reduction of the roughness maxima associated with standing-wave antinodes. Additionally, a very slight decrease in the background roughness is observed. These observations can be explained by the fact that the PEB induces acid diffusion throughout the entire resist thickness. Since diffusion is not restricted to regions corresponding to standing-wave antinodes, a slight smoothing effect is expected both at the roughness maxima and across the background level. The PEB conditions can be further optimized to enhance the smoothing effect, for example, by increasing the bake duration or operating at a slightly higher temperature. However, such optimization requires a careful trade-off: excessively high temperatures or prolonged bake times may induce over-diffusion of the photosensitive compounds, leading to a loss of vertical resolution, profile rounding, and modification of the step geometry. Despite the advantages of this technique, particularly its compatibility with the subsequent silicon etching process, allowing reduction of resist roughness without altering the already established etching workflow, its effectiveness remains limited. The PEB does not eliminate the standing waves; it only provides a global smoothing effect, moderately reducing the amplitude of roughness peaks while preserving the overall resist profile.

The second approach involves the use of a bottom anti-reflective coating (BARC), which, as mentioned in the introduction, has been extensively demonstrated in the literature as an effective method to suppress standing waves in photolithography. We fabricated two samples—one with and one without the BARC coating—following the same grayscale lithography process described earlier. For the BARC experiments, we employed the AZ BARLi II 90 formulation (supplied by Merck), spin-coated at 1500 rpm, which resulted in a film thickness of approximately 140 nm. The results are shown in Fig. 6.c, where the developed thickness is plotted as a function of the energy. The sample without BARC (blue curve) exhibits pronounced oscillations characteristic of standing-wave effects, while these oscillations are significantly reduced in the BARC-coated sample (yellow curve). This attenuation is attributed to the optical function of the BARC layer, which suppresses substrate reflections by absorbing the UV reflected radiation or introducing a phase shift that destructively interferes with it, thereby minimizing the formation of vertical interference patterns and ensuring a more uniform energy distribution through the resist thickness. The AFM

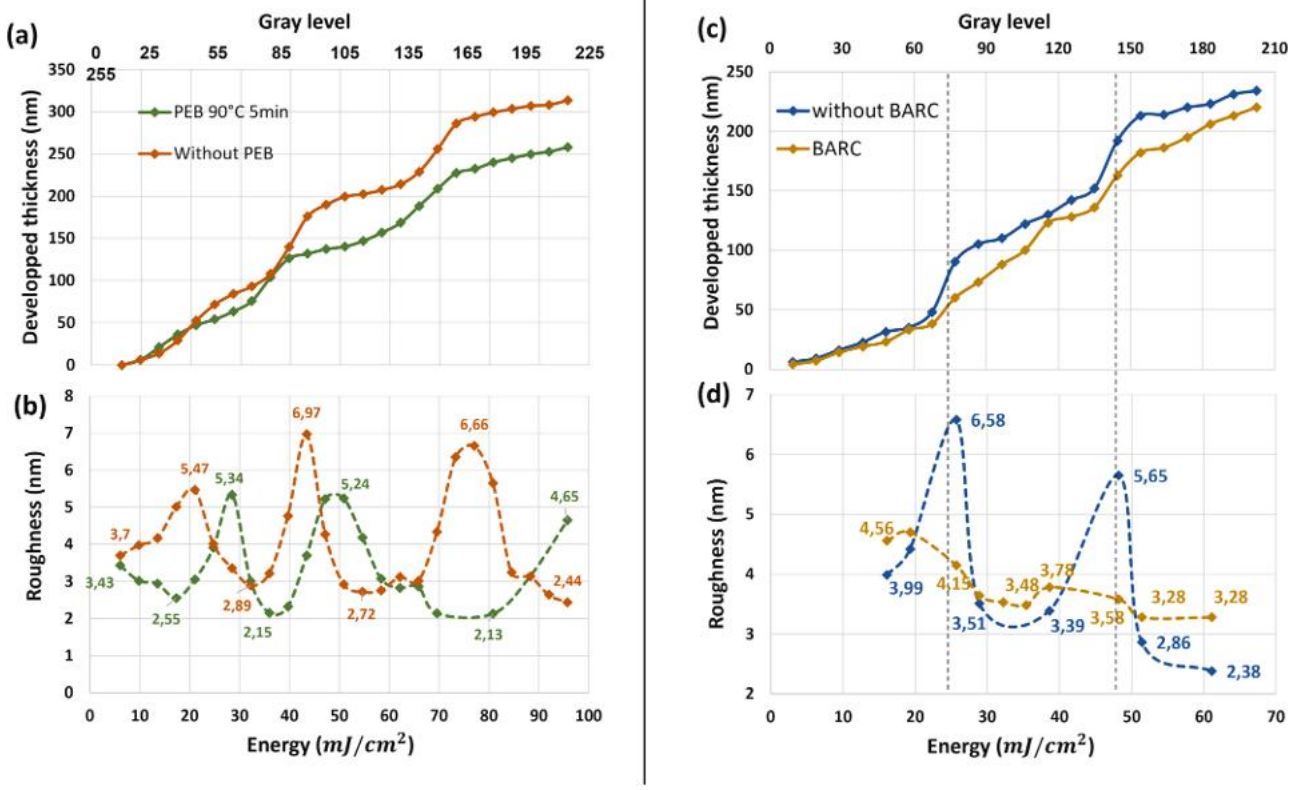


**Fig. 6.** (a) Comparison of contrast curves obtained for a sample subjected to a post-exposure bake (PEB at 90 °C for 5 min, green curve) and a reference sample without PEB (orange curve). (b) Corresponding AFM-measured surface roughness evolution for both samples. (c) Comparison of contrast curves obtained for a sample coated with a bottom anti-reflective coating (BARC, yellow curve) and a reference sample without BARC (blue curve). (d) Corresponding AFM-measured surface roughness evolution for both samples. (For interpretation of the references to colour in this figure legend, the reader is referred to the web version of this article.)

surface roughness measurements presented in Fig. 6.d further confirm this trend. The sample without BARC displays distinct roughness maxima at positions corresponding to standing-wave antinodes, reaching up to 6.58 nm compared to a baseline roughness of approximately 3 nm in regions between the peaks, whereas these peaks vanish completely when the BARC layer is used. This observation provides direct experimental evidence that the periodic variation of surface roughness originates from standing-wave interference within the photoresist, and that the introduction of a BARC layer efficiently suppresses this effect. However, in our case, the use of a BARC presents practical limitations. To transfer the staircase pattern into silicon, the etching of the BARC layer is necessary, thus requiring the development of another etching recipe. This would potentially affect the well-controlled resist-to-silicon selectivity achieved in our established fabrication process.

## 5. Conclusion

In this work, we have experimentally demonstrated that standing-wave effects in grayscale lithography play a direct and previously underexplored role in the generation of surface roughness in positive photoresists. Using one-dimensional staircase structures fabricated by maskless grayscale lithography, we showed that standing waves induce oscillations in the resist contrast curve and give rise to periodic roughness maxima that are systematically correlated with the steepest slopes of the swing-curve peaks. These roughness maxima occur in exposure dose regions where the dissolution rate is highest, making the resist surface particularly sensitive to local vertical dose non-uniformities. We further demonstrated that this roughness modulation is transferred into silicon during ICP etching, with an amplification of both background roughness and peak amplitudes due to the higher silicon etch rate. As a result, standing-wave effects in the resist directly govern the final silicon topography. Two strategies to mitigate standing-wave-induced roughness were investigated. Post-exposure bake (PEB) was shown to provide a modest global smoothing effect, slightly reducing both the roughness peaks and the background roughness, while preserving compatibility with the established silicon etching process. Quantitatively, the PEB results in an average reduction of approximately 19% in the roughness maxima and about 15% in the background roughness. However, PEB does not suppress standing waves and therefore cannot eliminate the roughness modulation. In contrast, the use of a bottom anti-reflective coating (BARC) effectively suppresses standing waves, leading to the complete disappearance of roughness maxima. Despite its effectiveness, the BARC approach introduces additional process complexity and etching constraints that limit its applicability in our current fabrication workflow. Overall, this study establishes a clear experimental link between standing waves, resist contrast behavior, and surface roughness in grayscale lithography. These observations provide key guidelines for the design and optimization of grayscale lithography processes where surface quality is critical. Additionally, they emphasize the importance of controlling optical interference effects when creating high-precision, three-dimensional microstructures.

## Declaration of competing interest

The authors declare the following financial interests/personal relationships which may be considered as potential competing interests:

Gourgon reports financial support was provided by European Commission. If there are other authors, they declare that they have no known competing financial interests or personal relationships that could have appeared to influence the work reported in this paper.

## Acknowledgement

This work was supported by the French RENATECH network and by the project "SCARBO next step - Space CARBon Observatory's solution to improve monitoring of GHG emissions and help establishing reliable data for emission trends forecasts (SCARBOn)", co-funded but the European Union under the Horizon Europe programme (Grant Agreement N°. 101135301).

## Appendix A. Supplementary data

Supplementary data to this article can be found online at https://doi.org/10.1016/j.mne.2026.100382.

## Data availability

No data was used for the research described in the article.

## References

[1] S.N. Khonina, N.L. Kazanskiy, M.A. Butt, Grayscale lithography and a brief introduction to other widely used lithographic methods: a state-of-the-art review, Micromachines 15 (2024) 1321.
[2] M.A. Smith, et al., Design, simulation, and fabrication of three-dimensional microsystem components using grayscale photolithography, J. Micro/Nanolithogr. MEMS MOEMS 18 (2019) 043507.
[3] J. Loomis, D. Ratnayake, C. McKenna, K.M. Walsh, Grayscale lithography—automated mask generation for complex three-dimensional topography, J. Micro/Nanolithogr. MEMS MOEMS 15 (2016) 013511.
[4] D.N. Shanks, T. Wenger, R.E. Muller, J.K. Wallace, D.W. Wilson, Metasurfaces with freely varying height in the visible using grayscale lithography, Nano Lett. 25 (38) (2025) 14090.
[5] Z. Guo, et al., Generation of perfect vortex beams with polymer-based phase plate, IEEE Photon. Technol. Lett. 32 (2020) 565–568.
[6] I.S. Garcia, et al., Nanoimprint lithography for grayscale pattern replication of mems mirrors in a 200 mm wafer, J. Manuf. Process. 116 (2024) 202–209.
[7] I.S. Garcia, et al., Fabrication of a mems micromirror based on bulk silicon micromachining combined with grayscale lithography, J. Microelectromech. Syst. 29 (2020) 734–740.
[8] C. McKenna, K. Walsh, M. Crain, J. Lake, Maskless direct write grayscale lithography for mems applications, in: IEEE (Ed.), 2010 18th Biennial University/Government/Industry Micro/Nano Symposium, 1–4, 2010.
[9] C.M. Waits, B. Morgan, M. Kastantin, R. Ghodssi, Microfabrication of 3d silicon mems structures using gray-scale lithography and deep reactive ion etching, Sensors Actuators A Phys. 119 (2005) 245–253.
[10] A. Bouchouri, M.N. Akram, P.A. Øhlckers, X. Chen, Optimization of grayscale lithography for the fabrication of flat diffractive infrared lenses on silicon wafers, Micromachines 15 (2024) 866.
[11] N. Allouti, et al., Grayscale lithography process study for sub 5µm microlens patterns, in: Novel Patterning Technologies for Semiconductors, MEMS/NEMS, and MOEMS 2019, SPIE, 2019, pp. 16–30, vol. 10958.
[12] F. Lima, I. Khazi, U. Mescheder, A.C. Tungal, U. Muthiah, Fabrication of 3d microstructures using grayscale lithography, Adv. Opt. Technol. 8 (2019) 181–193.
[13] J. Chrzanowska-Giżyńska, O. Śle˙zak, P. Nyga, M. Wankiewicz, Fabrication of infrared detector with monolithic microlens produced in thermal reflow process, Infrared Phys. Technol. 133 (2023) 104801.
[14] M.A. Mattelin, et al., Fabrication and replication of high efficiency blazed gratings with grayscale electron beam lithography and uv nanoimprint lithography, in: In Advanced Fabrication Technologies for Micro/Nano Optics and Photonics XIII vol. 11292, SPIE, 2020, 1129204.
[15] J. Deng, et al., Nonlinear optical information encoding with grayscale lithography enabled metasurfaces, Nano Lett. 25 (2025) 7450–7456.
[16] N. Gerges, et al., Optimized ultraviolet grayscale process for high vertical resolution applied to spectral imagers, J. Vac. Sci. & Technol. B 39 (2021).
[17] M. Yamamoto, H. Horibe, A. Sekiguchi, E. Kusano, S. Tagawa, Standing-wave effect in photoresist with and without hmds, J. Photopolym. Sci. Technol. 21 (2008) 299–304.
[18] C.A. Mack, Lithography on reflective substrates, Microlithogr. World 6 (1997) 21–22.
[19] M.K. Poutous, Z. Hosseinimakarem, E.G. Johnson, Photoresist surface roughness characterization in additive lithography processes for fabrication of phase-only optical vortices, J. Micro/Nanolithogr. MEMS MOEMS 11 (2012) 043009.
[20] J. Cunha, et al., Assessing tolerances in direct write laser grayscale lithography and reactive ion etching pattern transfer for fabrication of 2.5 d si master molds, Micro Nano Eng. 19 (2023) 100182.
[21] R. Kirchner, N. Chidambaram, M. Altana, H. Schift, How post-processing by selective thermal reflow can reduce the roughness of 3d lithography in micro-optical lenses, Laser 3D Manufacturing IV vol. 10095, SPIE, 2017, pp. 8–16.
[22] T. Yamaguchi, K. Yamazaki, H. Namatsu, Influence of molecular weight of resist polymers on surface roughness and line-edge roughness, J. Vac. Sci. & Technol. B 22 (2004) 2604–2610.
[23] B. Erbas, et al., Combining thermal scanning probe lithography and dry etching for grayscale nanopattern amplification, Microsyst. Nanoeng. 10 (2024) 28.
[24] I. Khazi, U. Muthiah, U. Mescheder, 3d free forms in c-si via grayscale lithography and rie, Microelectron. Eng. 193 (2018) 34–40.
[25] T. Kozawa, Relationship between stochastic effect and line edge roughness in chemically amplified resists for extreme ultraviolet lithography studied by Monte Carlo simulation, Jpn. J. Appl. Phys. 51 (2012) 086504.
[26] C.A. Mack, Reducing roughness in extreme ultraviolet lithography, J. Micro/Nanolithogr. MEMS MOEMS 17 (2018) 041006.
[27] S. Schermer, et al., Optimizing reticle-based high-throughput i-line grayscale projection lithography for 3D structures with low surface roughness, Micro Nano Eng. 38 (2025) 100319.
[28] H. Yao, et al., Bottom anti-reflective coating for hyper na process: theory, application and material development, Lithography Asia 2008. vol. 7140, SPIE, 2008.
[29] Microlight3d. https://www.microlight3d.com/. Accessed: 2025-11-17.
[30] C.A. Mack, Swing curves. Microlithogr, World 3 (1994) 23–25.
[31] C. Mack, Fundamental Principles of Optical Lithography: The Science of Microfabrication, John Wiley & Sons, 2008.